INL/JOU-25-80477-Revision-1

# Advanced Characterization of Metallic Fuels by Atom Probe Tomography

July 2025

Sohail Shah, Mukesh Bachhav, Anshul Kamboj, Tiankai Yao, Daniel J Murray, Arnold Pradhan, Luca Capprioti

Changing the World's Energy Future

Idaho National Laboratory

*INL is a U.S. Department of Energy National Laboratory operated by Battelle Energy Alliance, LLC*

INL/JOU-25-80477-Revision-1

# Advanced Characterization of Metallic Fuels by Atom Probe Tomography

**Sohail Shah, Mukesh Bachhav, Anshul Kamboj, Tiankai Yao, Daniel J Murray, Arnold Pradhan, Luca Capprioti**

**July 2025**

**Idaho National Laboratory**
**Idaho Falls, Idaho 83415**

**http://www.inl.gov**

**Prepared for the**
**U.S. Department of Energy**
**Under DOE Idaho Operations Office**
**Contract DE-AC07-05ID14517**

# High resolution microstructural, chemical studies and localized burnup analysis in an irradiated U-10Zr metallic fuel

Sohail Shah, Anshul Kamboj, Kourtney Wright, Daniele Salvato, Arnold Pradhan, Daniel J. Murray, Luca Capriotti, Tiankai Yao, Mukesh N. Bachhav*

[1] Nuclear Materials Performance Division, Idaho National Laboratory, Idaho Falls, ID, USA
*corresponding author: Mukesh.Bachhav@inl.gov

**Abstract**

This study involves high resolution characterization of a sodium bonded solid uranium (U)-10 wt.% zirconium (Zr) metallic fuel irradiated in Fast Flux Test Facility (FFTF). The fuel centerline temperature during irradiation was estimated to be around 675°C with the peak burnup 13.1 atomic percent. Samples for transmission electron microscopy (TEM) and atom probe tomography (APT) were prepared from different regions/zones in the fuel cross section radially to elucidate the microstructural changes and chemical redistribution of solute elements as well as fission products during irradiation experiment. TEM results indicate the irradiation in fast flux testing leads to the formation of extensive Zr-rich precipitates with varying sizes in the U-Zr fuel matrix. APT analysis performed to investigate redistribution of Zr, U and fission products along the radial direction of fuel pin showed Zr-rich precipitates entrapping the fission products in higher concentration as compared to the α-U phases. The local burnup ($^{235}$U depletion) is found to be consistent, calculated by quantification of $^{235}$U, $^{236}$U and $^{238}$U isotopes from mass spectrum obtained from APT along the radial direction. Zr-rich precipitation and its implication on fuel constitutional redistribution are discussed based on SEM, TEM and APT results.

Key words: *Metallic fuel, irradiation, uranium, zirconium, transmission electron microscopy, atom probe tomography, precipitation, isotopes.*

# 1. Introduction

Uranium alloyed with 10 wt. % Zirconium (U-10Zr) is a leading candidate for sodium-cooled fast reactors (SFRs) owing to its higher densities of fissile and fertile materials than most other fuel systems [1, 2]. The metallic U-Zr alloys also have excellent reactor core performance owing to high breeding ratio and low fissile inventory [1, 2]. Another advantage of metallic fuels is their relative easy fabrication with high thermal conductivity, capable of attaining high burnup close to 20% fissions per initial metal atom (FIMA) [3]. These fuels can also be recycled with multiple benefits such as confining actinides in the fuel cycle preventing high level nuclear waste generation. They have been extensively developed under various fuel development programs at Idaho National Laboratory (INL) since the 1950s [4]. Numerous irradiation experiments have been performed at FFTF, Experimental Breeder Reactor-II (EBR-II) and the Transient Reactor Test Facility (TREAT) [3-6] to test performance of structural materials and fuel performance [7-10].

The performance of U-10Zr fuel can be impacted by numerous issues like fission gas release causing fuel swelling in certain cases, which increases the fuel rods inner pressure [11]. Fuel cladding chemical and mechanical interaction (FCCI and FCMI), fuel swelling and Zr redistribution are the other fuel phenomena that can influence or limit fuel performance under several different conditions [2, 12-16]. The Zr redistribution impacts fuel performance as it influences the mechanical, physical and thermal properties of the fuel [13]. The effect of temperature and chemical potential gradients between different phase fields promotes different redistribution across the radial direction. The microstructure of the current irradiated fuel has been shown to exhibit three distinct concentric zones: a central Zr enriched zone, a uranium (U) enriched and Zr depleted intermediate zone and a slightly Zr enriched outer (periphery) zone [17]. The redistribution phenomena has been characterized in U-10Zr fuel [17] as well as a U-Pu-Zr fuel [18], although different conditions of irradiation forms distinct zones. Radial variation in thermal conductivity was commonly seen since each region had distinct microstructure with different phases impacting thermal properties [19]. Apart from microstructural and chemical changes within the fuel, burnup measurement is essential for nuclear fuel qualification and performance [20]. It is a direct assessment of energy produced during the fission process. It thus becomes crucial to estimate local burnup with high spatial resolution which is known to impact distribution of fission products both in the fuel and cladding region.

The development of advanced characterization capabilities and techniques has enabled the improved understanding of some representative metallic fuel cross-sections and the irradiation behavior on structural materials, ceramic and metallic fuels [14, 15, 21-31]. The site-specific sample preparation using the focused ion beam (FIB) allows high resolution characterization using probe corrected scanning transmission electron microscopy (STEM) coupled with Atom Probe Tomography (APT) to potentially quantify spatial variations of chemistry at the nanoscale. The APT technique is known to provide three-dimensional (3D) mapping of elements with atomic scale spatial resolution, allowing the characterization of different phases within the fuel [32]. A wide range of structural materials and fuels have been characterized using APT to elucidate the segregation at the interfaces and chemical composition of different phases [33-43]. With its high chemical resolution and sensitivity to isotopic composition, APT mass spectrums of nuclear fuels

can be utilized to determine the local burnup in irradiated fuels by the quantification of U isotopes [20].

In this work, systematic microstructural and chemical analysis is performed using APT and TEM on sodium (Na) bonded solid U-10Zr fuel irradiated to high burnup in the FFTF reactor along the radial direction [44, 45]. The redistribution of Zr is examined along with fuel phases and qualitative distribution of solid fission products (SFPs) at the end of irradiation using 3D distribution from APT. Burnup estimation at different regions within the fuel is also estimated using isotopic information from mass spectrum of APT. This multimodal characterization method is aimed to improve the understanding of irradiation induced microstructural changes in U-Zr fuel along with chemical identification and distribution of fission products in solid metallic fuels.

## 2. Materials and Methods

### 2.1 Fuel pin

The fuel cross-section being analyzed is from a U-10Zr (10 wt.%, 22 at.% Zr) fuel pin that has an approximate length of 91.4 cm and a diameter of 0.498 cm contained between two to three fuel slugs cast by a counter gravity vacuum method [44]. The irradiation was a part of the Mechanistic Fuel Failure (MFF) series for metallic fuels conducted in the FFTF [44, 45]. The MFF-3 assembly consisted of 169 U-10Zr fuel pins reaching a peak burnup of 13.1 at.% [14]. The sample analyzed in the current study is pin #193114 taken from axial location of x/L=0.44. The HT-9 cladding (ferritic/martensitic) tubes have an inner diameter of 0.574 cm and an outer diameter of 0.686 cm resulting in a smear density of close to 75% (smear density is defined as the cross-sectional areal ratio of the fuel slug to the inner cladding surface). The $^{235}$U enrichment is 32.4 wt.% for this fuel [17]. The sample preparation for post irradiation examination is carried out in the hot cell facility details of which can be found in reference [17]. Additional details on the fuel/cladding fabrication, chemistry and geometry can be found in [14, 17].

### 2.2 Irradiation condition of fuel pin

The burnup, inner cladding temperature and time averaged fuel centerline temperatures were estimated using BISON simulations and are summarized in Table 1. The detailed calculated profiles can be found elsewhere [14]. The inner cladding temperature was 530°C while the fuel centerline temperature was 675°C extracted at 0.44L of pin 193114. The peak burnup was estimated at 13.1 at. % FIMA (Fissions per Initial Metal Atom). More detailed information on irradiation of fuel pin can be found in reference [14] along with irradiation details for other fuel pins performed in the MFF-3 campaign.

Table 1. Summary of irradiation condition of the fuel analyzed in the current study.

| Axial height | Burnup (at. %) | Time averaged linear power (W/cm) | Time averaged fuel centerline temperature (°C) | Time averaged inner cladding temperature (°C) |
|---|---|---|---|---|
| 0.4 | 13.1 | 562 | 675 | 530 |

### 2.3 Surface imaging and sample preparation

The polishing and surface characterization of fuel pin was performed at the IMCL facility. The samples were loaded in a shielded focused ion beam (FIB) instrument (FEI G3 Helios plasma) attached to an inert glove box, for imaging and marking sites for APT and TEM. The surface imaging of the pin was carried out using back-scattered electrons (BSE) and energy dispersive x-ray spectroscopy (EDS) is performed on the entire cross section of the fuel to reveal different phases across the pin radius. BSE imaging was carried out at 30 kV voltage and a beam current of 1.6 nA. EDS acquisitions were carried out at 20 kV voltage with a beam current of 6.4 nA. The high energy xenon (Xe) beam was used to prepare site specific TEM and APT lamella involving ion trenching, polishing and lift-outs. The final thinning and sharpening of TEM and APT samples was done using the FEI Quanta 3D FIB with Ga beams at 30 kV and various currents. Final low 2 kV cleaning was performed on lamella and needle shaped tips to minimize the beam damage for TEM and APT analysis.

### 2.4 High resolution characterization

APT and TEM studies are performed systematically along the radial direction of the irradiated U-10Zr pin by making specimen close to each other to compare microstructural evolution shown in Figure 1. The FEI (now thermofisher) Talos TEM was used for bright field imaging and scanning-TEM energy dispersive spectroscopy (STEM-EDS) analysis. The net intensities collected on the STEM-EDS maps were converted to at. % maps using the Velox software. The samples from irradiated U-10Zr for APT were prepared by the standard lift out and milling process using the Quanta 3D field emission gun (FEG) focused ion beam (FIB) [46]. The LEAP 5000 XR instrument at IMCL facility was used to collect data in laser mode with a pulse energy of 50 pJ and a pulse repetition rate of 125 kHz. The data was collected at a rate of 5 atoms per 1000 pulses. The detection efficiency of the LEAP system is 50%. All samples were cooled to cryogenic temperature of 55 K before data acquisitions started. Data analysis was done using CAMECA Integrated Visualization and Analysis Software (IVAS) 3.8.16. Reconstructions were performed following the standard voltage reconstruction protocol. Mass spectrum fitting is performed using MATLAB code developed for U isotope quantification [47].

## 3. Results and Discussion

### 3.1 Fuel constituent redistribution at SEM scale

An SEM overview of the fuel section at low magnification is seen in Figure 1. The SEM-EDS results clearly show a distinct three zone redistribution of the irradiated fuel as defined in a previous study [17]. For visual aid, Zone 1 and Zone 2 are demarcated by dashed lines in Figure 1 mainly consisting of the central zone and the intermediate zone respectively. As can be seen from Figure 1, the Zr concentration is the highest in Zone 1 and the lowest in the Zone 2 with intermediate Zr content in Zone 3.

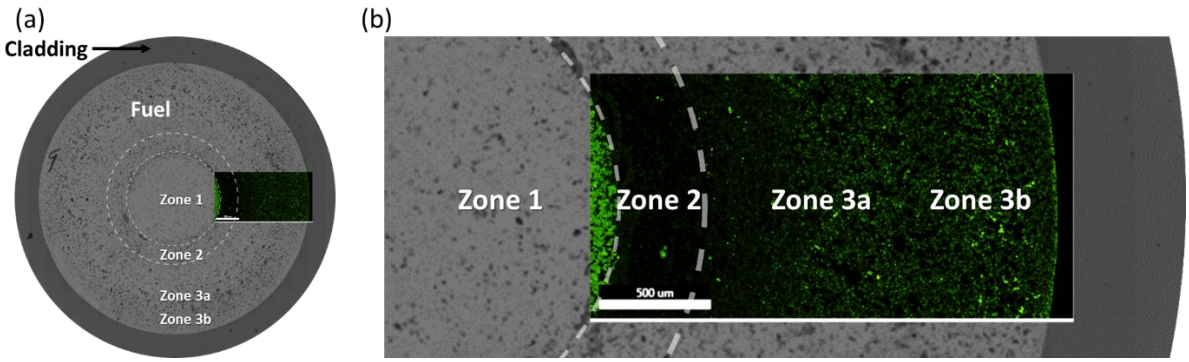


***Figure 1.*** *(a) Backscattered electron (BSE) image of the U-10Zr fuel cross section and (b) EDS of Zr elemental mapping in green superimposed on the fuel cross section image [17].*

Zone 1 extends from the center of the fuel pin to 0.32R where 'R' is the pin radius. Zone 2 is defined from 0.32R to 0.45R while Zone 3 extends from 0.48R to 1.00R. Zone 3 can be subdivided into two zones namely Zone 3a and Zone 3b, mainly classified by the slightly higher Zr concentrations in Zone 3b. It should be noted that SEM-EDS mappings as shown in Figure 1 is only a qualitative assessment of Zr distribution across the fuel pin cross-section. However, these micrographs clearly show redistribution of Zr (shown in green) in each region.

Zone 1 in Figure 2(a-c) shows an increased level of heterogeneity with the co-existence of multiple sub-phases. The contrast differences clearly reveal two different phases populating Zone 1. Presence of porosity throughout Zone 2 is indicated in Figure 2(d-f). Zone 3 in Figure 2(g-l) also indicates numerous, large and irregularly shaped pores. Migration of Zr atoms is caused by the radial temperature gradients (675 °C-550 °C) encompassing a multi-phase regime. Experiments and modelling efforts suggest three radial zones to be formed in solid U-Zr fuels when the hottest part of the fuel operates at temperatures exceeding the α-U + γ2 to β-U + γ2 transition (662 °C) [30, 48]. Under these conditions, the temperature (thermal) and chemical potential gradients across the pin radius will induce the diffusion of Zr from the coldest part of the β-U + γ2 region into the hotter central region. This central region may operate either in the β-U + γ2 phase field (if the centerline temperature is below 693 °C) or in the γ phase field (if the centerline temperature is above 693 °C), resulting in the former being depleted of Zr (Zone 2) and the latter being enriched in Zr (Zone 1). Thermal gradient caused within the fuel is purely a thermo-physical process. Due to the power production in the solid cylinder (fuel pin) and the exchange of heat with a medium on the outside (fuel pin → cladding → sodium coolant), there is a parabolic temperature profile throughout the radius, with the highest temperature at the center and the lowest temperature at the surface.

Fission gas pores (FGP) appear to be dark due to sectioned polished planes. The SEM greyscale image (Figure 2) was processed in ImageJ to set a threshold, making the pores appear black and the non-porous regions white (Figure S4). MATLAB was then used to quantify the area fraction, which is the ratio of the area covered by pores to the total area of a specified zone within the fuel pin cross-section. The areas of circular regions corresponding to 0-0.32R and 0.48R-R were computed, and Zone 1 had an area fraction of 0.1 while Zone 3 had an area fraction of 0.37. Zone 3 has the highest number density of these large irregular shaped pores as seen in Figure 2(g-l). Zone 1 has the least number of pores while the

characterization of pores in Zone 2 is hindered due to lower concentration of Zr. The high U content in Zone 2 leads to increased surface degradation due to the formation of oxides, which adversely affects the surface texture [45]. Previous studies on the same fuel [17] yielded qualitative mapping of solid fission products (SFP) in and around the FGP. These are found to be in the size range of 1-30 μm. Higher magnification TEM and APT characterizations are performed to further investigate the nanoscale precipitates and quantify the distribution of fission products around these precipitates. The locations chosen for TEM and APT lift outs are highlighted for each zone in Figure 2. Specimens for TEM and APT for high resolution studies are prepared close to each other to ensure direct comparison of microstructural features. Zone 1 lift outs are highlighted in red while Zone 2 and Zone 3 lift outs are shown in black and blue respectively. These are not to scale and are shown to provide an overview of the regions being characterized in the following sections. The fuel and cladding gap closed due to rapid fuel swelling which is a common characteristic of U-Zr fuels as seen in Figure 2(m-o). This is also seen in Na bonded solid fuel pins having a smear density of 75% and burnups of approximately 1-2 at.% [3, 14, 49]. The time averaged fuel centerline temperature was 675 °C and the time averaged inner-cladding temperature was 550 °C. TEM characterization of the FCCI region with the cladding can be found in another study [14].

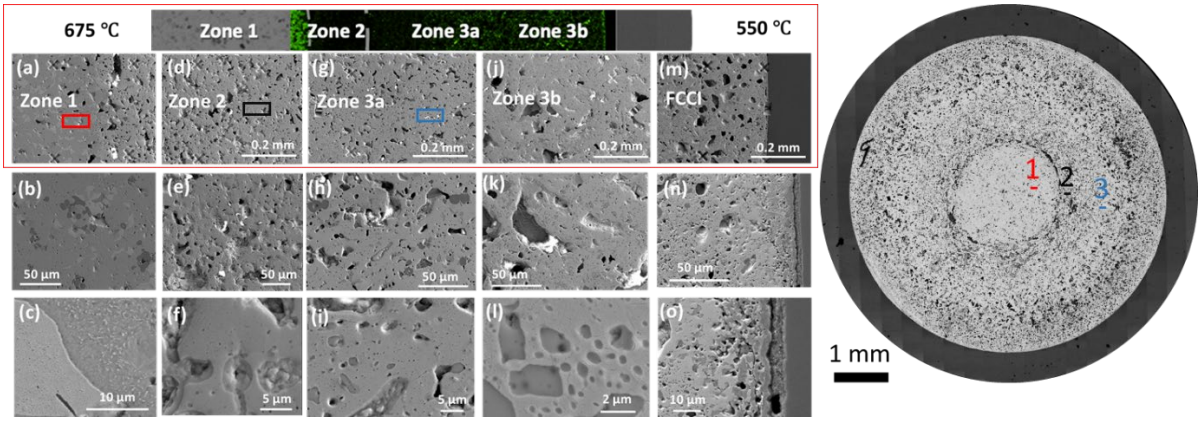


***Figure 2****. (a) Low magnification SEM micrographs from the radial section of the fuel pin with higher magnification images showing the microstructure for (a-c) Zone 1, (d-f) Zone 2, (g-l) Zone 3 and (m-o) FCCI region. Regions marked on the BSE images and the fuel overview image for TEM and APT lift outs as red: Zone 1, black: Zone 2 and blue: Zone 3.*

### 3.2 Transmission Electron Microscopy

Zr redistribution has been previously observed in U-Pu-Zr fuels at different burnups and for different Zr content [50-53]. The radial distribution largely consists of depletion in Zr at the central part of the fuel while the outer region of the fuel has Zr concentration close to the pre-irradiated nominal composition, however this strongly depends on temperature gradient across the fuel pin and irradiation conditions [50]. Since the fuel pin operated between temperature of 550 °C to 675 °C, there is a possible co-existence of up to five different phase fields [54]. The Zr inventory is balanced by the presence of Zr rich secondary phases/precipitates which is the primary focus of this study. They are distributed across the fuel pin cross-section from Zone 1 to 3. Zone 1 has characteristic sizes ranging from 30-150 nm with an average size of approximately 75 nm

dispersed in the U-rich matrix as seen in Figure 3(a-c). Zone 2 is characterized with similar Zr-rich nano-precipitates found in the matrix enriched in U and characteristic sizes ranging from 20-70 nm with an average size of approximately 40 nm. Zone 3 has similar precipitates although the density of these precipitates appeared to be higher than Zone 1 and 2 as seen in Figure 3(g-i). Figure 3(d-f) clearly shows inhomogeneous distribution of Zr and U along the grain boundary. Zone 2 has Zr enrichment at grain boundaries with U depletion. This Zr rich microstructural feature maybe a consequence of radiation induced segregation (RIS). Additionally, a denuded zone of Zr can be seen around the larger precipitate seen in Zone 3 (Figure 3g-i) with higher concentrations of U along the periphery of the precipitate marked with red circle. Similar trends are seen for the smaller sized Zr precipitates presented in the following APT sections. The EDS spectra for the mapped regions in Figure 3 can be found as supplementary figure S1. Selected area electron diffraction (SAED) in Zone 1 indicates that the nanoscale Zr-rich precipitates are bcc $\gamma_2$, as indicated by the patterns outlined in green in Figure 4. SAED collected from the surrounding U-rich matrix indicated orthorhombic α-U as shown by the pattern outlined in yellow in Figure 4. Larger Zr precipitates in the order of microns are also seen in Zone 3 as highlighted in the red circle in Figure 3(i). These are indexed as bcc $\gamma_2$ from the previous study [17]. Possible Zr diffusion outwards from Zone 2 could be causing higher Zr concentrations in Zone 3. However, due to the simultaneous occurrence of multiple phenomena, providing a substantial explanation for this occurrence is challenging. There is a combination of temperature, irradiation, crystallography and chemistry all playing a part. Separate effect studies (both in-situ experiments and simulations e.g. Molecular Dynamics and/or phase field) to isolate possible precipitate (formation) kinetics mechanisms that is ruling this phenomenon will aid in understanding.

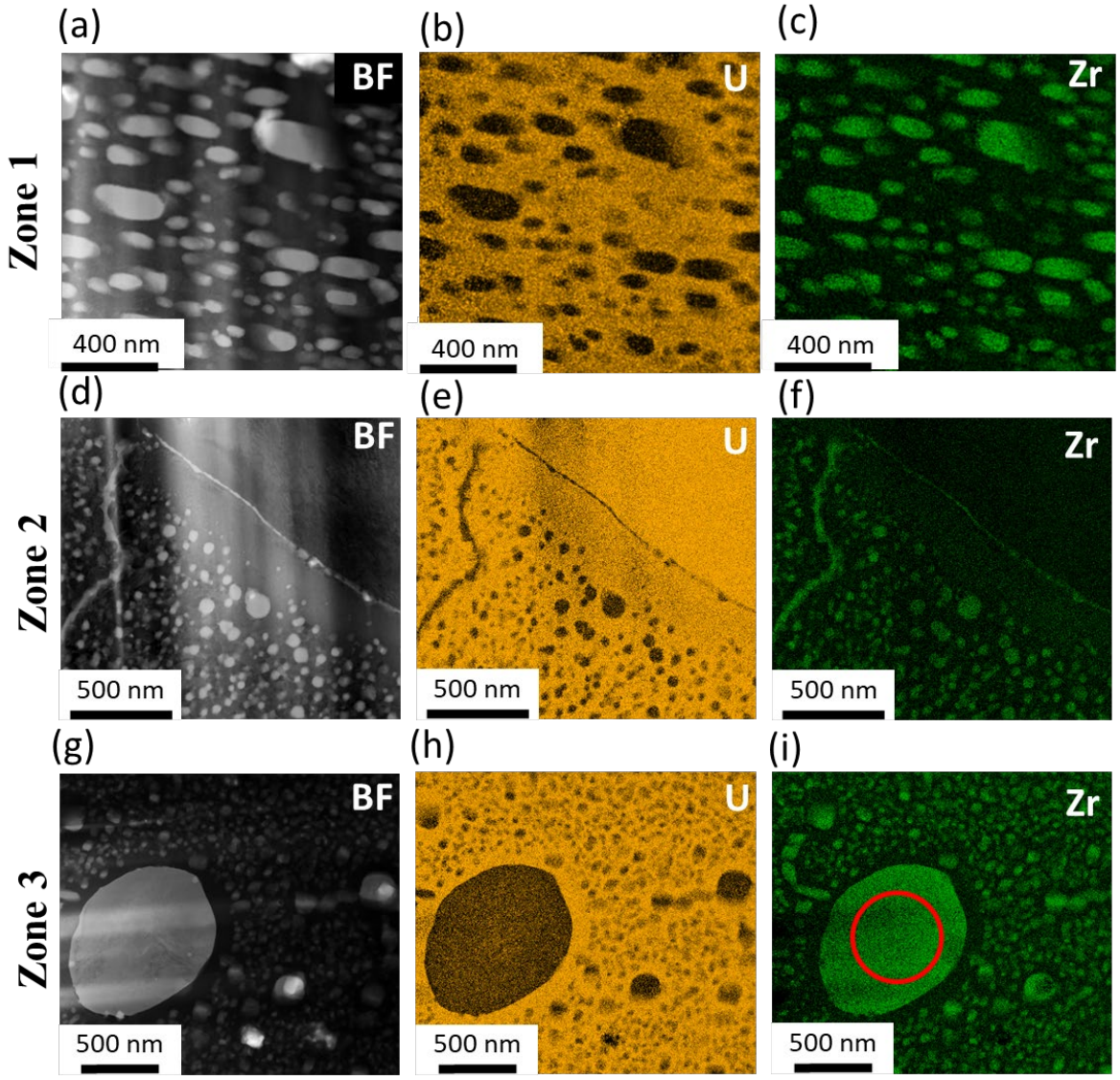


***Figure 3.*** *TEM analysis of different regions across the fuel pin cross-section. Bright field (BF) images and the corresponding EDS mapping of U in yellow and Zr in green for (a-c) Zone 1, (d-f) Zone 2 and (g-i) Zone 3.*

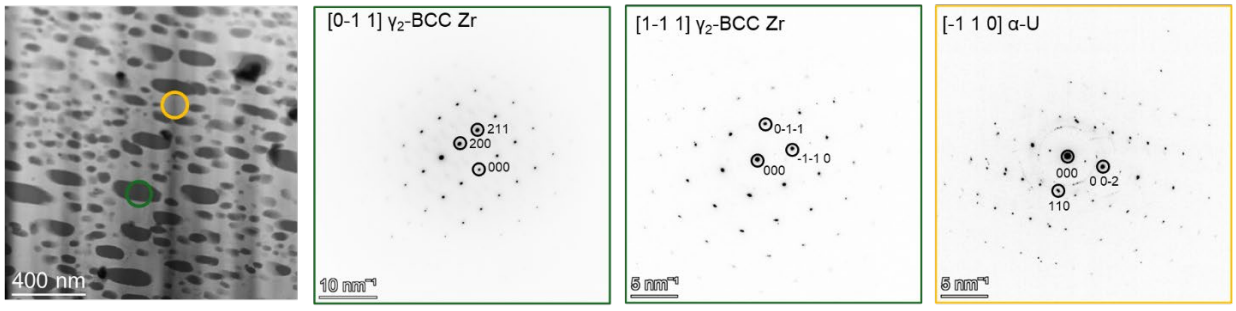

***Figure 4**. Selected area electron diffraction (SAED) patterns obtained from Zr rich precipitates in Zone 1 indicating a body centered cubic (bcc) crystal structure while the pattern from the matrix indicated orthorhombic α-U.*

### 3.3 Atom Probe Tomography

APT specimens were prepared from the same location as for TEM along the radial direction discussed above. Figure 5(a) shows a sliced (12 nm) APT reconstructions from Zone 1 with atom maps of U, Zr, Ru and molybdenum (Mo). Based on 3D reconstruction atom map, it is evident that solute elements U and Zr are non-uniformly distributed in the analyzed APT volume. Two distinct regions include a Zr enriched phase depleted in U and a matrix mainly enriched with U. A similar microstructural change has been previously reported for U-10Zr metallic fuels [55, 56]. A Zr iso-concentration map is used for visualization of Zr-rich precipitates as seen in Figure 5 for APT tips from Zone 1. These are nanoscale precipitates, with characteristic sizes ranging between 25-80 nm in agreement with TEM results (Figure 3). The precipitates are mainly spherical in shape with a few larger precipitates in a more globular shape. Based on proximity histogram (proxigram) shown in Figure 5(b) taken across Zr-rich precipitates, the Zr content was found to be around 80 at.% and U content close to 10 at.%. There are substantial amounts (~10 at.%) of fission product concentrated within these Zr enriched features. The fission products identified in the mass spectrum of irradiated U-10Zr are Sr, Ba, Pd, Ru, Ce, Pr, Mo, Kr, Rh, Cd, In and Nd (mass spectrum is provided in supplementary figure S2). For simplicity, all fission products are labelled as one group ‘FP’ in the proxigram plots except Ru and Mo (plotted separately) due to higher concentrations as compared to other fission products and was highly concentrated within the Zr enriched precipitates. Distribution of minor fission products can be found in the Supplementary Information S3.The Ru atom map in Figure 5(b) along with the proxigram clearly shows the enrichment inside these Zr enriched precipitates. It can be noted that Ru and Mo concentration increases near the interface of these precipitates indicating segregation near the interface of these Zr precipitates. Additionally, it should be noted that not all compounds and fission products observed were present during current post irradiation examination. The current fuel was characterized after 30 years of cooling time, by which many of the fission products originally present may have decayed.

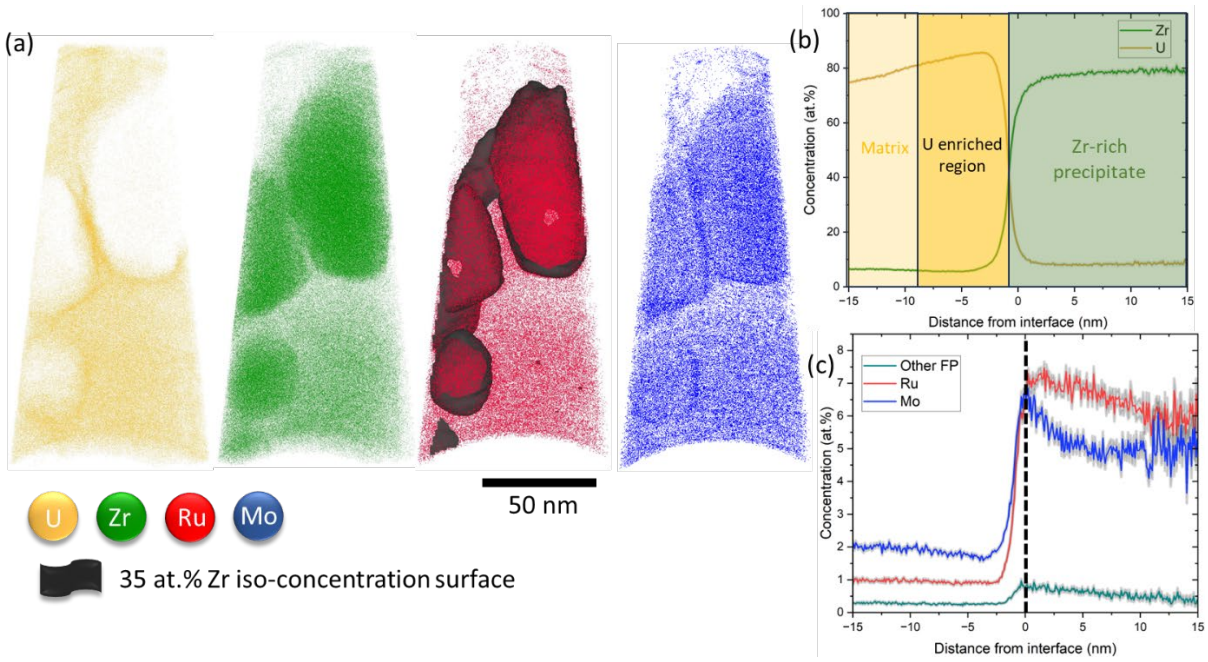


***Figure 5.*** *Sliced APT reconstruction of Zone 1 showing (a) major element atom maps (U in yellow and Zr in green) along with an iso-concentration map of 35 at. % Zr (in black) with Ru atom map in red and Mo in blue. Corresponding proxigram plots showing (b) Zr and U and (c) distribution of fission products across the Zr precipitate interfaces. The slice thickness is 12 nm.*

Zone 2 had a similar microstructure as Zone 1 with Zr enriched precipitates dominating within the U matrix demonstrated in Figure 6. The sliced region from the APT reconstructions shown in Figure 6 is 15 nm thick. The size of the Zr enriched precipitates ranged from 30 to 85 nm in diameter. A very similar trend in distribution of the fission products is observed when compared to Zone 1 wherein the concentration of these FPs is high inside the precipitates as observed in the proxigram. This proxigram is computed by taking an average from all Zr-rich precipitates. With the formation of these large Zr precipitates, the nearby Zr concentration dropped before stabilizing to the bulk concentration. This is highlighted in both Figure 5(b) and Figure 6(b) proxigrams wherein there is a Zr denuded zone around 10-15 nm away from the precipitate interface into the U matrix. The opposite trend is observed for U, wherein there is a slight enrichment near the interface of these precipitates before stabilizing to the bulk concentration away from the precipitates. This essentially translates into three distinct regions: a Zr rich region that corresponds to the Zr precipitates, a U rich region sFuel cladding chemical and mechanical interaction panning ~10 nm near the interface of these precipitates and the matrix region. These regions are distinctively seen in Zone 1 and 2 as seen in Figure 5 and Figure 6. The fission products are also enriched at the interface of the Zr-rich precipitates as seen in both proxigrams in Figure 5 and Figure 6. Zone 2 indicates Mo enrichment close to 15 at.% within the Zr rich precipitates, much higher than Zone 1. A clear three phase region can be defined across the precipitate region. The fuel matrix is close to pure U indicating α-U (close to 100% U) as seen in Figure 7 with the Zr concentration close to 0.2-0.4 at.%, consistent with previous results [17]. This is below the

solubility limit (0.5 at.% Zr) in the α- U phase at 662ºC [57, 58]. The Zr-rich precipitates are highly enriched with fission products, mainly Mo and Ru as seen from Figure 6 proxigrams across Zr precipitates. Quantification by atomic concentration profiles and proxigrams reveals a Zr concentration close to 75- 80% within the core of these precipitates as seen from Figure 5, Figure 6, Figure 7 and Figure 8. This can be due to the metastable nature of precipitates formed due to irradiation and fission products being found in these phases. This is slightly higher than the stoichiometric composition of $UZr_2$ indicating that these are not δ- $UZr_2$. Similar to zone 1, there is distinct segregation of Mo and other fission products near the interface of these Zr rich phases.

Consistent with Zone 1 and Zone 2, Zone 3 is dominated with similar microstructural features. Zr-rich precipitates are uniformly distributed throughout the APT dataset as seen in Figure 8(a) (sliced region is 15 nm thick). However, the number density of the larger precipitates is visibly lower as compared to Zone 1 and 2. Additionally, there are smaller Zr-rich precipitates on the order of 5-10 nm in size. These are absent in Zone 1 and 2 wherein the microstructure was dominated by the relatively larger Zr precipitates. This may be caused due to the temperature gradient across the fuel pin as seen in Figure 2 with a temperature difference of 125 °C from Zone 1 to Zone 3. A probable coarsening of these precipitates has taken place in Zone 1 and Zone 2 as compared to zone 3 where smaller precipitates are observed at a lower temperature zone. These observations pertain to the Zr rich precipitates observed within the APT datasets. However, as seen in Figure 3, larger (bcc $\gamma_2$) precipitates were also seen in Zone 3. Since the field of view in APT is not as large as TEM or SEM, it fails to give an overview of the entire microstructure. The smaller Zr precipitates seen in Zone 3 (Figure 8) are also enriched with around 75 at. % of Zr and 8-10 at.% of U with fission products accounting for the remaining 10-15 at.%. The denuded zone of Zr and enrichment of U around the larger Zr precipitates is absent in Zone 3 as seen in Figure 8(b). Consistent with zone 2, concentration of Mo within the Zr rich precipitates is higher as compared to Ru and other fission products. No diffraction spots were identified for these nano Zr precipitates in the previous study [17]. However, the overall similar morphology and chemical composition of these Zr precipitates indicates that they are the same phase and confirmed by TEM in the current studies as bcc $\gamma_2$ phase for Zone 1. Care must be taken when comparing these results to the overall Zr redistribution across the fuel pin cross-section since these are small APT volumes used for Zr precipitates and fission products quantification and not representative of the entire zone.

Iron (Fe) impurities are also observed within the APT datasets. These are mainly introduced into the system during the fabrication process. Fe is present in both phases (α- U and Zr-rich precipitates), although its concentration was slightly higher within the Zr precipitates (~0.1 at.%). The spatial distribution of Fe can be found in the Supplementary Information (S3).

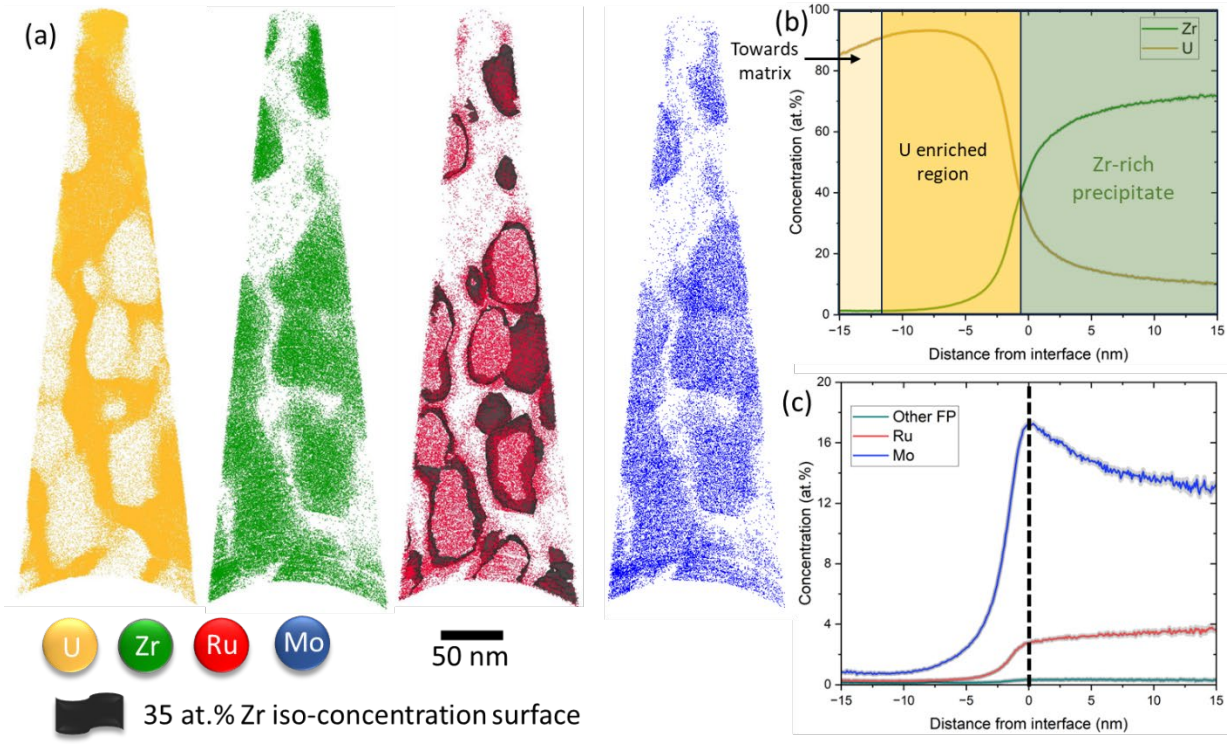


***Figure 6***. *Sliced APT reconstruction of Zone 2 tip showing (a) major element atom maps (U in yellow and Zr in green) along with an iso-concentration map of 35 at.% Zr (in black) with Ru atom map in red and Mo in blue. Corresponding proxigram plots showing (b) Zr and U and (c) distribution of fission products across the Zr precipitate interfaces. The slice thickness is 15 nm.*

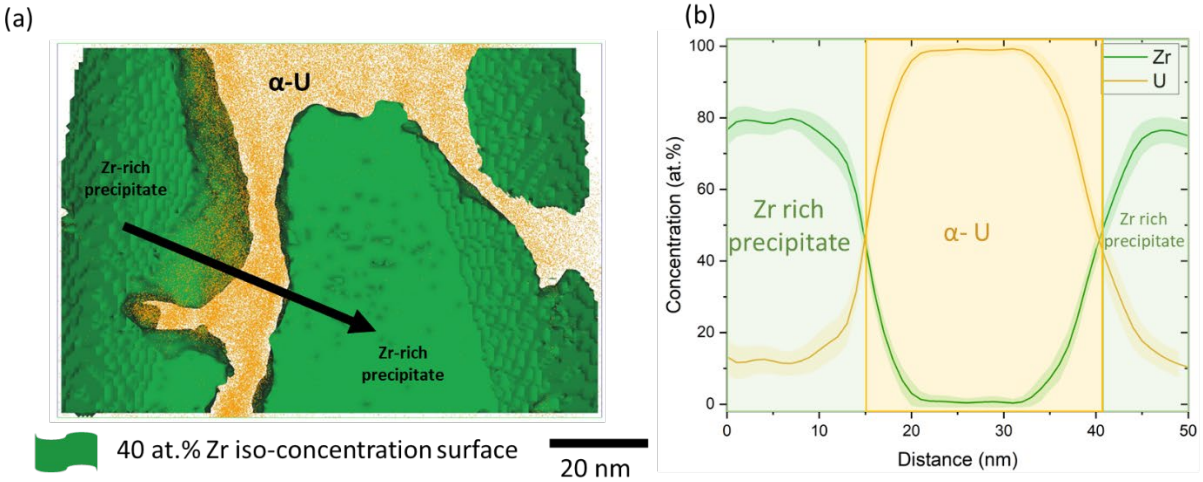


***Figure 7***. *1-D concentration profile of a cylinder (shown as a black arrow) with a diameter of 20 nm across Zr precipitates and U rich region in Zone 2. APT dataset clearly showing the Zr-rich precipitate and the α-U fuel matrix. The fission products distribution is very similar to proxigram estimates seen in* Figure 5, Figure 6 and Figure 8.

Characterization of fission products is essential in the assessment of fuel performance under varying irradiation conditions as it is the primary contributor to fuel swelling. Solid fission products are also responsible for the chemical attack on claddings commonly seen in U-Pu-Zr and U-Zr metallic fuel. This can lead to an increase in local cladding stress, limiting the life of fuel [59]. As seen from the APT figures, most of the Zr precipitates have Ru and Mo as the primary fission products. Previously, ZrRu precipitates were observed in ternary U-Pu-Zr and U-Pu-Zr-MA (minor actinides) fuels [50, 52, 60]. Depending on the location within the fuel sample, the ZrRu precipitates are associated with different fission products within the fuel interiors. The majority of these Zr precipitates are interconnected which was not straightforward to visualize in the APT maps of Figure 5, Figure 6 and Figure 8. Although majority of the solid fission products are accumulated within the FGP, which is much larger in size compared to these nanoprecipitates, it is interesting to note that elemental mapping clearly shows the fission products being entrapped within Zr-rich precipitates. Multiple studies on binary systems of U-Ru and U-Mo obtained from thermal analysis have been carried out previously suggesting low solubility of Ru and Mo in α-U (<0.5 at.%) [61, 62]. Many of the fission products identified within the current work are transition metals and chemically similar (Mo, Ru, Rh), indicating that due to low solubility of these elements in α-U, they possibly precipitated out of α-U and segregated to regions enriched with Zr during phase transformation. To the best of the authors knowledge, direct kinetic studies on the solubility and mobility of these fission products in U-Zr systems is sparse and is worth investigating in future studies.

The complementary techniques used within this study (SEM/TEM/APT) observe similar trends at reducing scale, though there are some differences due to the changing nature of the field of view and resolution. This is mainly due to the small region being analyzed by APT which focused mainly on the chemical distribution across Zr nano precipitates and not the entire zone. This study aims at studying the chemistry of the high number density of nano Zr precipitates along with fission product distribution across the α-U matrix and Zr rich regions which is extremely challenging to quantify using the TEM due to large uncertainty from the convoluted EDS signal for small precipitates embedded in the matrix. This study is significant for the qualification of advanced reactors as it provides a deeper understanding of the microstructural changes and constituent redistribution within metallic U-Zr fuel during irradiation. One of the primary challenges with the U-Zr fuel system is understanding the effects of temperature gradients and irradiation conditions on the redistribution of elements such as Zr and U. These redistributions can significantly impact the fuel's performance (thermal properties), integrity (mechanical properties), and overall safety during reactor operation. Constituent redistribution in metallic alloy fuels causes radial changes in phase compositions, impacting local power production and resulting in variations in irradiation behavior such as swelling, fission product generation/distribution, and mechanical, physical and thermal properties. Understanding and predicting this behavior is crucial for interpreting overall fuel performance during operation. Our findings provide initial groundwork for future analysis of phase evolutions and their implications on microstructure and mechanical/thermal properties. This information enhances our understanding of metallic fuel performance and aids in designing improved fuels for advanced nuclear reactors.

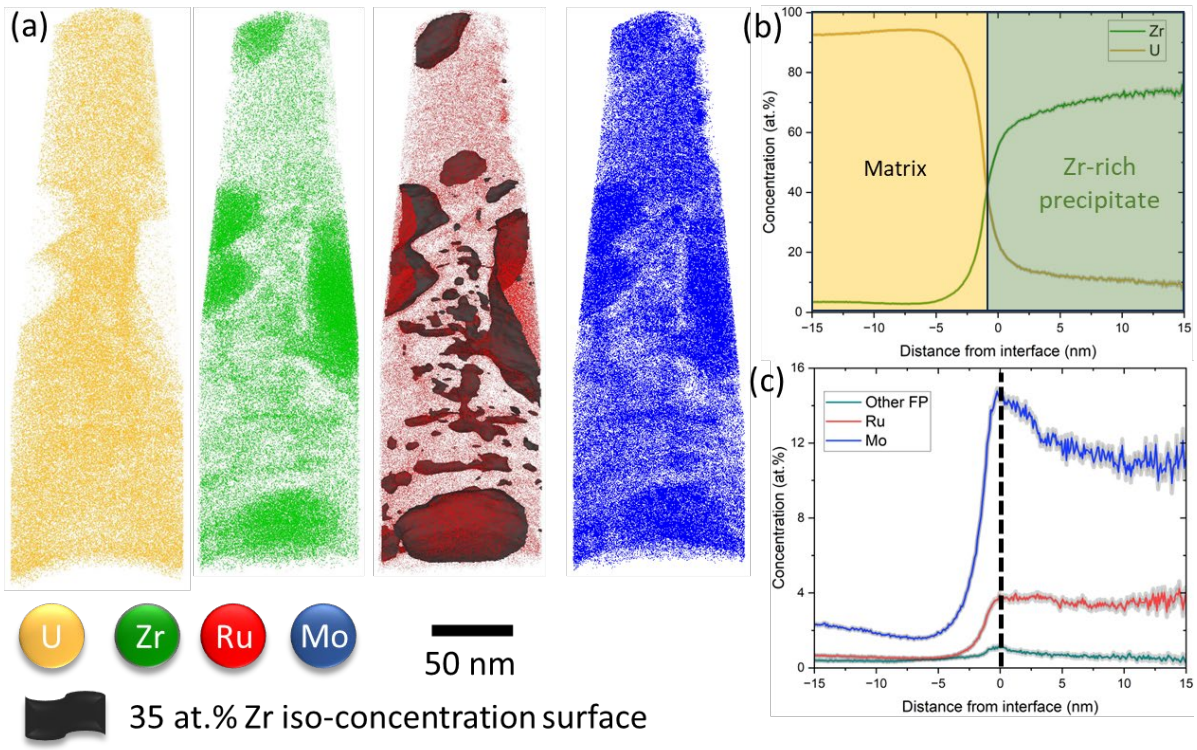


***Figure 8***. *APT reconstruction of Zone 3 showing (a) major element atom maps (U in yellow and Zr in green) along with an iso-concentration map of 35 at. % Zr (in black) with Ru atom map in red and Mo in blue. Corresponding proxigram plots showing (b) Zr and U and (b) distribution of fission products across the Zr precipitate interfaces. The slice thickness is 13 nm.*

### 3.4 $^{235}$U consumption estimation by APT

The burnup of nuclear fuel is related to the energy produced per mass of fuel and directly impacts the fission product production and fuel microstructural evolution. It is essential to predict the changes in fuel microstructure and composition as a function of burnup for the safe operations of the reactor. The qualification and performance of the fuel is also assessed based on several parameters: the burnup being one of them making it an important parameter for nuclear fuels. Different methods have been used previously to determine the burnup of irradiated fuels such as gamma spectroscopy [63-66], plasma atomic emission spectroscopy [67, 68] and wet chemistry methods [69-71]. These methods each have limitations and merits for accurate quantification. Some of the methodologies use fission products like $Nd^{148}$ and its different isotopes as a suitable candidate for burnup estimation. This is due to Nd not being radioactive and it can be determined by isotope dilution mass spectroscopic methods [71]. However, the above-mentioned methodologies are time-consuming and expensive. Additionally, these methods create substantial amounts of radiological waste, and the consistency of burnup measurements depends on an accurate quantification of fission yields. Previously, the local burnup of fresh and irradiated fuels for both intermediate and high burnup was estimated using APT quantification of U isotopes [20].

The atom probe allows the quantification of local variation of chemistry with high spatial resolution and can be applied to different isotopes in the case of nuclear fuels.

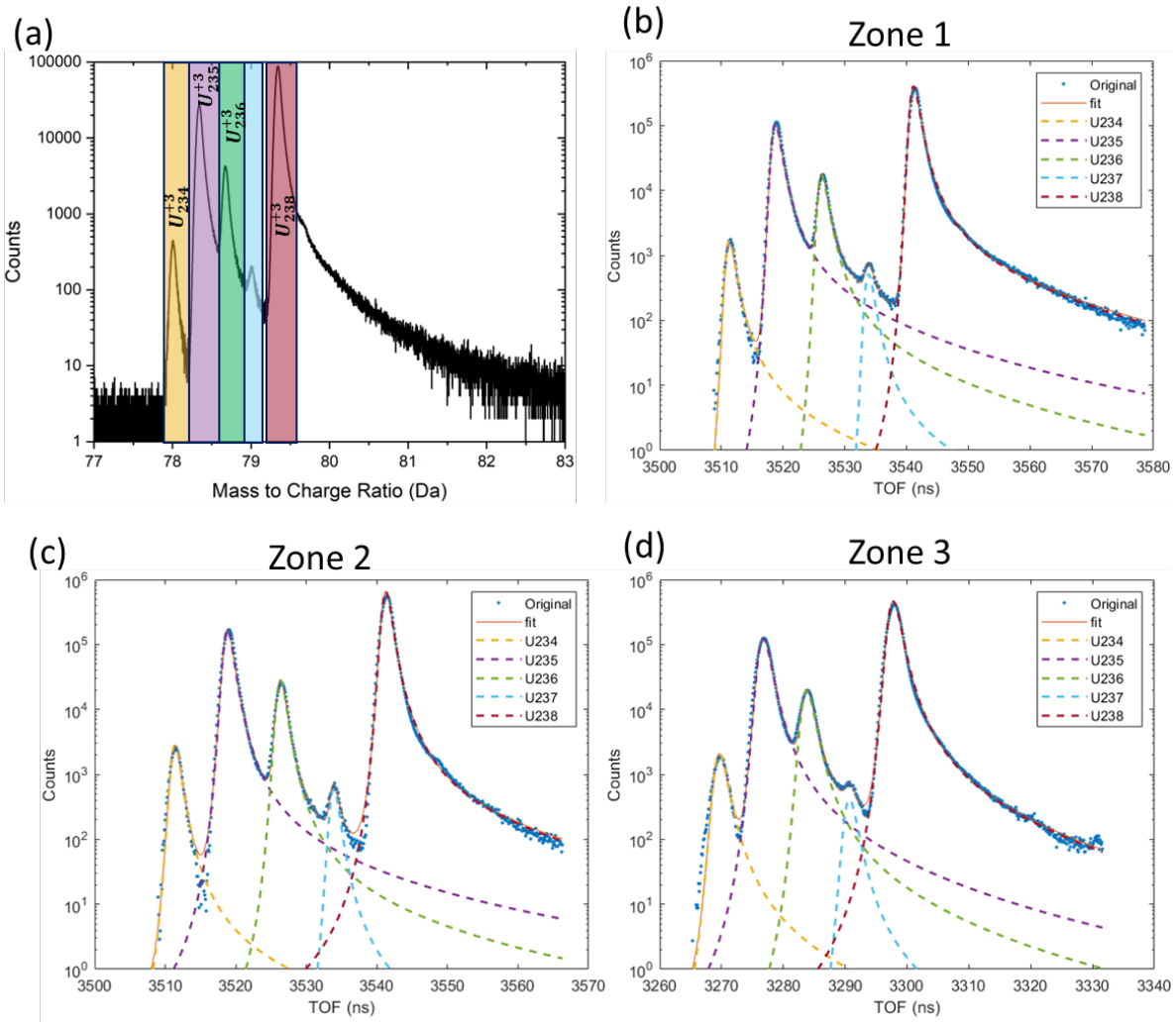


***Figure 9***. *(a) Schematic of burnup analysis estimation using mass spectrum of APT dataset. Individual peak identification and fitting for (b) Zone 1, (c) Zone 2 and (d) Zone 3.*

In the present study, the local consumption of $^{235}U$ in Zone 1, 2 and 3 is determined using the $U^{3+}$ isotopes. Specifically, $U^{3+}$ isotopes are used for the quantification although $U^{2+}$ charge state in the APT mass spectrum has better peak separation and isotopic identification. The $U^{2+}$ charge state is avoided due to the overlapping peaks of hydrides from the $^{234}U$ isotope. This implies that $^{235}U^{2+}$ will have a hydride contribution from $^{234}U^{2+}$ making deconvoluting complicated. When considering $U^{3+}$ charge state, there is no peak overlap with hydrides and the peaks can be easily separated as seen in Figure 9. Previous studies have estimated the $U_{235}$ consumption which implies the ratio of $^{235}U$ consumed by fission to the $^{235}U$ present at the beginning of life. This is commonly referred to as the burnup for the Materials Test Reactor (MTR) fuels [20].

However, for Gen IV reactors metallic fuels, the burnup is reported in terms of fissions per initial metal atoms (FIMA) or the ratio of the amount of $^{235}$U that is consumed to the sum of $^{235}$U and $^{238}$U present at the beginning of life. In order to convert the enrichment into a more representative $^{235}$U consumption value as reported in [14], we must multiply it with the initial enrichment and is given as follows:

$$U_{235}\ consumption = \frac{\left[\frac{U_{235}/U_{total}}{U_{238}/U_{total}}\right]_{BOL} - \left[\frac{U_{235}+U_{236}/U_{total}}{U_{238}/U_{total}}\right]_{EOL}}{\left[\frac{U_{235}/U_{total}}{U_{238}/U_{total}}\right]_{BOL}} * \left[U_{235}/U_{235}+U_{238}\right]_{BOL} \quad (1)$$

where $\left[U_{235}/U_{235}+U_{238}\right]_{BOL}$ is the enrichment of the fuel and EOL is the end of life. The beginning of life (BOL) ratio for $^{235}$U and $^{238}$U are extracted from the initial enrichment of $^{235}$U mentioned in Section 2.1.

The calculated $U_{235}$ consumption using equation (1) is 36.5 ± 0.2 % for Zone 1, 41.3 ± 0.2 % for Zone 2 and 33.5 ± 0.2 % for Zone 3 indicating that the consumption does not vary much from one zone to the other while the microstructure is evolving. We utilize the calculated $U_{235}$ consumption in Equation (2) to compare it with the simulated burnup estimations as reported in [14]. The corresponding burnup values for Zone 1, 2 and 3 is 11.82 at. %, 13.39 at. % and 10.84 at. % respectively. However, care must be taken while interpreting these results since APT data acquisitions for the current fuel are performed in laser mode resulting in a prominent thermal tail for $U_{238}^{3+}$ observed in various other alloy systems [72, 73]. Previous studies [20] showed voltage mode offered significantly lower background noise and thermal tails (delayed signal) as compared to laser mode. The presence of thermal tail contributes to the background close to the mass peaks. It is observed that $U_{238}^{3+}$ is particularly sensitive to the burnup estimation using equation 2) based on its range. Additionally, the burnup is computed on small APT volumes and was not representative of the entire Zr redistribution for different zones as seen in Figure 1.

An in-house developed dynamic peak fitting toolbox is applied to systematically disentangle the distinct contributions of individual uranium isotopes. More details about the toolbox can be found in this paper [74]. This tool employs statistical methodologies, incorporating both Johnson and Cauchy probability distribution functions (PDFs) replicating the nuanced peak shapes observed in APT across different operational modes, such as voltage and laser settings. Specifically, the Cauchy distribution is selected to emulate symmetrical peaks associated with voltage mode, while the Johnson distribution is tailored to effectively capture the thermal tail characteristic of laser mode peaks. The relative weighting of each distribution is based on the initial peak morphology, thereby minimizing the fitting error. The dynamic peak fitting toolbox employs a systematic four-step process for the deconvolution of overlapping peaks. First, unsampled raw time-of-flight (TOF) data is obtained from the acquired APT dataset. Subsequently, the second step involved the estimation and subtraction of background signals from the TOF data. The third step includes the identification, isolation, and amalgamation of overlapping peaks into discrete regions of interest.

The final step involves the deconvolution process, elucidating the individual contribution of each peak within the designated region of interest. These four steps resulted in the quantification of counts corresponding to individual peaks, as prominently depicted in Figure 9 b-d. The counts associated with individual peaks are used for subsequent burnup calculations. Considering the uncertainties both from the burnup estimations and Byson simulations, a reasonable agreement between the values is reported here further supporting the use of APT as a technique to quantify the burnup not only for the MTR fuels but also for Gen IV metallic fuels.

The formation of Zr redistribution is a known phenomenon in multiple Zr fuels such as U-Zr and U-Pu-Zr, however, experimental evidence is scarce [18, 30, 45]. From previous studies, it was inferred that temperature gradient plays an important role in the formation of redistribution zones across the fuel pin. Burnup appears to have a negligible role in dictating the redistribution as seen in this study. All three zones showed similar $^{235}U$ consumption and fission product distribution with variations in microstructural features. This in turn indicates the burnup to be similar in the three Zones and hence the Zr redistribution is mainly attributed towards temperature gradient than burnup. Additionally, previous studies have also shown maximum Zr concentration in the center zone (Zone 1) at very low burnups (5 at.%) [48] indicating redistribution is relatively rapid and essentially complete by 5 at.% burnup. This confirms the effect of temperature and time to be key factors in determining the different zone distribution as indicated in other studies [45, 48]. The high-resolution characterization of Zr-rich nanophases in this study provides valuable insights into the fission product distribution across Zr-rich phases seen throughout the fuel pin generating an accurate description of the U-10Zr fuel behavior under irradiation along with fuel development and qualification of advanced reactors.

## 4. Conclusions

In conclusion, the high-resolution nanoscale microstructural characterization of Zr redistribution in a Na-bonded solid U-10Zr fuel pin irradiated in the FFTF reactor was carried out using SEM, TEM and APT. In addition to microstructural studies, chemical analysis of fission products and U isotope quantification were conducted using mass spectrometry from APT. The study identified Zr-rich nano precipitates across all three zones, with Zone 2 showing the highest volume fraction. These precipitates, embedded within a U-rich α-U matrix, contained high concentrations of fission products such as Ru and Mo, which increased with the volume fraction of the precipitates. The relatively constant $^{235}U$ concentration throughout the fuel pin suggests that Zr redistribution is primarily driven by temperature gradient rather than by $^{235}U$ consumption due to fission reactions. This research enhances the understanding of the different phases within the fuel pin and supports the development of thermodynamic models to better predict U-10Zr fuel behavior under various irradiation conditions. This study provides essential data for modeling and simulation efforts to predict the long-term performance and ensure the safe operation of nuclear fuels.

Disclosure statement

## 5. Acknowledgement:

This work was supported by the U.S. Department of Energy, Office of Nuclear Energy under DOE Idaho Operations Office Contract DE-AC07- 05ID14517 as part of Nuclear Science User Facilities award 23-4774. MB acknowledge the support of Nuclear Science User Facilities scientific technique and expertise development activities.

## 6. References

1. Di Lemma, F.G., et al., *Postirradiation characterization of palladium as an additive for fuel cladding chemical interaction mitigation in metallic fuel.* Journal of Nuclear Materials, 2022. **558**: p. 153403.
2. Ogata, T., Y.S. Kim, and A. Yacout, *Metal fuel performance modeling and simulation.* 2020.
3. Hofman, G.L., L.C. Walters, and T. Bauer, *Metallic fast reactor fuels.* Progress in nuclear energy, 1997. **31**(1-2): p. 83-110.
4. Crawford, D.C., D.L. Porter, and S.L. Hayes, *Fuels for sodium-cooled fast reactors: US perspective.* Journal of Nuclear Materials, 2007. **371**(1-3): p. 202-231.
5. Bauer, T., et al., *Behavior of metallic fuel in TREAT transient overpower tests*. 1988, Argonne National Lab.
6. Carmack, W., et al., *Metallic fuels for advanced reactors.* Journal of Nuclear Materials, 2009. **392**(2): p. 139-150.
7. Walters, L., *Thirty years of fuels and materials information from EBR-II.* Journal of nuclear Materials, 1999. **270**(1-2): p. 39-48.
8. Mariani, R.D., et al., *Metallic fuels: The EBR-II legacy and recent advances.* Procedia Chemistry, 2012. **7**: p. 513-520.
9. Pitner, A. and R. Baker, *Metal fuel test program in the FFTF.* Journal of Nuclear Materials, 1993. **204**: p. 124-130.
10. Dickerman, C., et al., *TREAT meltdown of irradiated metallic fast-reactor fuel in an inert atmosphere.* Nuclear Applications, 1967. **3**(8): p. 461-473.
11. Guo, J., et al., *Fission Gas Behaviors and Relevant Phenomena in Different Nuclear Fuels: A Review of Models and Experiments.* Frontiers in Energy Research, 2022. **10**: p. 766865.
12. Inagaki, O., K. Nakamura, and T. Ogata, *Progress in Understanding of Fuel-Cladding Chemical interaction in Metal Fuel.* 2013.
13. Williams, W., et al., *Assessment of swelling and constituent redistribution in uranium-zirconium fuel using phenomena identification and ranking tables (PIRT).* Annals of Nuclear Energy, 2020. **136**: p. 107016.

14. Salvato, D., et al., *The effect of temperature and burnup on U-10Zr metallic fuel chemical interaction with HT-9: A SEM-EDS study.* Journal of Nuclear Materials, 2024. **591**: p. 154928.
15. Wang, Y., et al., *Transmission electron microscopy characterization of the fuel-cladding chemical interactions in HT9 cladded U-10Zr fuel.* Journal of Nuclear Materials, 2022. **572**: p. 153990.
16. Pradhan, A., et al., *Characterization of Fuel Cladding Chemical Interaction on a High Burnup U-10Zr Metallic Fuel via Electron Energy Loss Spectroscopy Enhanced by Machine Learning.* Materials Characterization, 2024. **218**: p. 114524.
17. Salvato, D., et al., *Transmission electron microscopy study of a high burnup U-10Zr metallic fuel.* Journal of Nuclear Materials, 2022. **570**: p. 153963.
18. Kim, Y.S., et al., *Modeling of constituent redistribution in U–Pu–Zr metallic fuel.* Journal of Nuclear Materials, 2006. **359**(1-2): p. 17-28.
19. Chen, W. and X.-M. Bai, *Temperature and composition dependent thermal conductivity model for U-Zr alloys.* Journal of Nuclear Materials, 2018. **507**: p. 360-370.
20. Bachhav, M., et al., *A novel approach to determine the local burnup in irradiated fuels using Atom Probe Tomography (APT).* Journal of Nuclear Materials, 2020. **528**: p. 151853.
21. Di Lemma, F., et al., *In-situ TEM Studies of Microstructural and Phase Evolution in Metallic Fuel Alloys*, in *Materials in Nuclear Energy Systems (MiNES 2023)*. 2023.
22. Tang, Y., et al., *Segmentation and classification of fission gas pores in reactor irradiated annular U10Zr metallic fuel using machine learning models.* Materials Characterization, 2024: p. 114061.
23. Xu, F., et al., *Advanced characterization-informed machine learning framework and quantitative insight to irradiated annular U-10Zr metallic fuels.* Scientific Reports, 2023. **13**(1): p. 10616.
24. Wang, Y., et al., *Small-scale mechanical testing and characterization of fuel cladding chemical interaction between HT9 cladding and advanced U-based metallic fuel alloy.* Journal of Nuclear Materials, 2022. **566**: p. 153754.
25. Mayweg, D., et al., *Limits of hydrogen analysis by atom probe tomography targeting Zr (Fe, Cr) 2 second phase particles in Zr-based fuel cladding from reactor operation.* Journal of Nuclear Materials, 2024. **601**: p. 155343.
26. Eriksson, J., et al., *An atom probe tomography study of the chemistry of radiation-induced dislocation loops in Zircaloy-2 exposed to boiling water reactor operation.* Journal of Nuclear Materials, 2021. **550**: p. 152923.
27. Motta, A.T., A. Couet, and R.J. Comstock, *Corrosion of zirconium alloys used for nuclear fuel cladding.* Annual Review of Materials Research, 2015. **45**(1): p. 311-343.
28. Curtis, N., et al., *Local chemical ordering of a neutron-irradiated CrFeMnNi compositionally complex alloy.* Acta Materialia, 2025: p. 120752.
29. Harp, J., et al., *NON-DESTRUCTIVE POST IRRADIATION EXAMINATION OF FIRST CYCLE ACCIDENT TOLERANT AND ADVANCED ZIRCONIUM ALLOY HIGH BURNUP FUEL RODS.* 2024, Oak Ridge National Laboratory (ORNL), Oak Ridge, TN (United States).
30. Hirschhorn, J., et al., *A study of constituent redistribution in U–Zr fuels using quantitative phase-field modeling and sensitivity analysis.* Journal of Nuclear Materials, 2019. **523**: p. 143-156.
31. Thomas, J., et al., *Transmission electron microscopy investigation of phase transformation and fuel constituent redistribution in neutron irradiated U-10wt.% Zr fuel.* Journal of Nuclear Materials, 2023. **581**: p. 154443.
32. Sen, A., et al., *Irradiation Effects on Stability of δ-UZr2 phase in U-50 wt% Zr Alloy.* Journal of Nuclear Materials, 2023. **576**: p. 154251.
33. Marquis, E.A., *Atom probe tomography applied to the analysis of irradiated microstructures.* Journal of Materials Research, 2015. **30**(9): p. 1222-1230.
34. Reese, E.R., et al., *Dose rate dependence of Cr precipitation in an ion-irradiated Fe18Cr alloy.* Scripta Materialia, 2018. **146**: p. 213-217.
35. Bachhav, M., G.R. Odette, and E.A. Marquis, *α′ precipitation in neutron-irradiated Fe–Cr alloys.* Scripta Materialia, 2014. **74**: p. 48-51.

36. Bachhav, M., G.R. Odette, and E.A. Marquis, *Microstructural changes in a neutron-irradiated Fe–15 at.% Cr alloy.* Journal of Nuclear Materials, 2014. **454**(1-3): p. 381-386.
37. Shah, S., et al., *Effect of cyclic ageing on the early-stage clustering in Al–Zn–Mg (-Cu) alloys.* Materials Science and Engineering: A, 2022. **846**: p. 143280.
38. Shah, S., et al., *Precipitation, mechanical properties and early slant ductile fracture in cyclic and naturally aged Al-Zn-Mg (-Cu) alloys.* Materials & Design, 2022. **222**: p. 111026.
39. Shah, S., et al., *On the Use of a Cluster Identification Method and a Statistical Approach for Analyzing Atom Probe Tomography Data for GP Zones in Al–Zn–Mg (–Cu) Alloys.* Microscopy and Microanalysis, 2023: p. ozad133.
40. Miller, B., et al., *Evidence of Xe-incorporation in the bubble superlattice in irradiated U-Mo fuel.* Journal of Nuclear Materials, 2023. **587**: p. 154743.
41. Arivu, M., et al., *Atom probe tomography of segregation at grain boundaries and gas bubbles in neutron irradiated U-10 wt% Mo fuel.* Materials Letters, 2024: p. 136414.
42. Shah, S., et al., *Correlating microstructure and mechanical properties of harvested high dose Zorita light water reactor internals.* Journal of Nuclear Materials, 2024. **599**: p. 155241.
43. Shah, S., et al., *Irradiation-induced formation of G-phase precipitates and M2X carbides in self-ion irradiated HT-9.* Nuclear Instruments and Methods in Physics Research Section B: Beam Interactions with Materials and Atoms, 2025. **563**: p. 165703.
44. Carmack, W.J., et al., *Metallography and fuel cladding chemical interaction in fast flux test facility irradiated metallic U-10Zr MFF-3 and MFF-5 fuel pins.* Journal of Nuclear Materials, 2016. **473**: p. 167-177.
45. Harp, J.M., et al., *Scanning electron microscopy examination of a Fast Flux Test Facility irradiated U-10Zr fuel cross section clad with HT-9.* Journal of Nuclear Materials, 2017. **494**: p. 227-239.
46. Miller, M.K., et al., *Review of atom probe FIB-based specimen preparation methods.* Microscopy and microanalysis, 2007. **13**(6): p. 428-436.
47. Bachhav, M., et al., *Automated Burnup Analysis from Metallic, Ceramic, and Amorphous Fuels using Atom Probe Tomography.* Microscopy and Microanalysis, 2024. **30**(Supplement_1).
48. Hofman, G., S. Hayes, and M. Petri, *Temperature gradient driven constituent redistribution in U □ Zr alloys.* Journal of nuclear materials, 1996. **227**(3): p. 277-286.
49. Keiser, D.D., *3.15-metal fuel-cladding interaction*, in *Comprehensive Nuclear Materials: Volume 1-5*. 2012, Elsevier. p. 423-441.
50. Brémier, S., et al., *Electron probe microanalysis of a METAPHIX UPuZr metallic alloy fuel irradiated to 7.0 at.% burn-up.* Journal of Nuclear Materials, 2016. **480**: p. 109-119.
51. Rahn, T., et al., *Investigation of constituent redistribution in U-Pu-Zr fuels and its dependence on varying Zr content.* Journal of Nuclear Materials, 2021. **557**: p. 153301.
52. Capriotti, L., et al., *Characterization of metallic fuel for minor actinides transmutation in fast reactor.* Progress in Nuclear Energy, 2017. **94**: p. 194-201.
53. Matthews, C., et al., *Fuel-cladding chemical interaction in U-Pu-Zr metallic fuels: A critical review.* Nuclear Technology, 2017. **198**(3): p. 231-259.
54. Yao, T., et al., *Understanding spinodal and binodal phase transformations in U-50Zr.* Materialia, 2021. **16**: p. 101092.
55. Shah, S., et al., *Advanced Characterization of Metallic Fuels by Atom Probe Tomography*. 2024, Oxford University Press US.
56. Pradhan, A., S. Shah, and M. Bachhav, *Atom Probe Tomography (APT) Characterization of Annular U-Zr Metallic Fuel Cladded with HT-9.* Microscopy and Microanalysis, 2024. **30**(Supplement_1).
57. Sheldon, R. and D. Peterson, *The U-Zr (uranium-zirconium) system.* Bulletin of Alloy Phase Diagrams, 1989. **10**(2): p. 165-171.
58. Yao, T., et al., *The advanced characterization, post-irradiation examination, and materials informatics for the development of ultra high-burnup annular U-10Zr metallic fuel.* Frontiers in Nuclear Engineering, 2023. **1**: p. 1050262.

59. Inagaki, O., K. Nakamura, and T. Ogata. *Progress in understanding of fuel-cladding chemical interaction in metal fuel*. in *International Conference on Fast Reactors and Related Fuel Cycles: Safe Technologies and Sustainable Scenarios (FR13). Presentations*. 2013.
60. Keiser, D., *Fuel-cladding interaction layers in irradiated U-ZR and U-PU-ZR fuel elements*. 2006, Argonne National Lab.(ANL), Argonne, IL (United States).
61. Mason, R.E. and M.S. El-Genk, *Experimental investigation of the ruthenium-uranium and rhenium-uranium binary systems.* Journal of nuclear materials, 1994. **217**(3): p. 304-321.
62. Saller, H., F. Rough, and D. Vaughan, *The constitution diagram of uranium-rich uranium-molybdenum alloys*. 1951, Battelle Memorial Inst., Columbus, OH (United States).
63. Mitsui, H., *Burnup Analysis of Uranium Dioxide Nondestructive Analysis by External Conversion Method.* Journal of Nuclear Science and Technology, 1966. **3**(11): p. 491-495.
64. Lebrun, A. and G. Bignan, *Nondestructive assay of nuclear low-enriched uranium spent fuels for burnup credit application.* Nuclear Technology, 2001. **135**(3): p. 216-229.
65. Popa, P., M.D. Coster, and D. Langela, *Burnup determination of nuclear fuels by high resolution gamma spectrometry, track formation in solid-state detectors, and neutron dose measurements.* Nuclear Applications and Technology, 1970. **9**(5): p. 755-761.
66. Kim, J.S., et al., *Analysis of high burnup pressurized water reactor fuel using uranium, plutonium, neodymium, and cesium isotope correlations with burnup.* Nuclear Engineering and Technology, 2015. **47**(7): p. 924-933.
67. Giglio, J., et al., *Determination of burnup in spent nuclear fuel by application of fiber optic high-resolution inductively coupled plasma atomic emission spectroscopy (FO-HR-ICP-AES).* Nuclear Instruments and Methods in Physics Research Section A: Accelerators, Spectrometers, Detectors and Associated Equipment, 1997. **396**(1-2): p. 251-256.
68. Lee, C.H., et al., *Separation of fission products from spent pressurized water reactor fuels by anion exchange and extraction chromatography for inductively coupled plasma atomic emission spectrometric analysis.* Analytica Chimica Acta, 2001. **428**(1): p. 133-142.
69. Sivaraman, N., et al., *Burn-up measurements on nuclear reactor fuels using high performance liquid chromatography.* Journal of radioanalytical and nuclear chemistry, 2002. **253**: p. 35-40.
70. Guéguen, F., et al., *Multi-elemental Gd, Eu, Sm, Nd isotope ratio measurements by liquid chromatography coupled to MC-ICPMS with variable Faraday cup configurations during elution.* Talanta, 2017. **162**: p. 278-284.
71. Rider, B., et al., *DETERMINATION OF $ sup 148$ Nd IN IRRADIATED URANIUM AND PLUTONIUM AS A MEASURE OF BURNUP*. 1967, General Electric Co., Pleasanton, Calif. Nuclear Technology Dept.
72. Bachhav, M., et al., *Investigation of wüstite (Fe1− xO) by femtosecond laser assisted atom probe tomography.* Ultramicroscopy, 2011. **111**(6): p. 584-588.
73. Bachhav, M., et al., *Evidence of lateral heat transfer during laser assisted atom probe tomography analysis of large band gap materials.* Applied Physics Letters, 2011. **99**(8).
74. al., A.K.e., *Precision burnup assessment through dynamic peak fitting in atom probe tomography for metallic and ceramic fuel analysis.* Microscopy and Microanalysis, 2024.